ELSEVIER

Experimental and numerical study of developed flow and heat transfer in coolant channels with 45 degree ribs

B. Bonhoff [a,*], S. Parneix [a], J. Leusch [a], B.V. Johnson [a], J. Schabacker [b], A. Bölcs [b]

[a] *ABB Corporate Research Ltd., Segelhof, CH-5405, Baden-Dättwil, Switzerland*
[b] *Swiss Federal Institute of Technology, EPFL-LTT, Lausanne, Switzerland*

Abstract

The flow characteristics within coolant channels were investigated experimentally and numerically to assess the current capability of Navier–Stokes codes to predict flow and heat transfer in coolant passages. The assessment was made for developed flows in a stationary square coolant channel with opposing square ribs staggered and angled at 45 degrees to the duct centerline, with rib heights of 10% of the channel height and with a Reynolds number of 50 000. A stereoscopic digital PIV measurement system was assembled to simultaneously measure all three-velocity components in narrow sheets. The instantaneous PIV data were averaged to obtain the three mean velocities and the six Reynolds stresses. Velocity and heat transfer distributions were calculated for developed flow in one segment of the ribbed channels by applying cyclic boundary conditions. The calculations were made with three sets of wall and turbulence models: (1) a standard k–ϵ turbulence model with wall functions, (2) a differential-Reynolds-stress turbulence model with wall functions and (3) a standard k–ϵ turbulence model with a two-layer wall model. The comparison between the measurements and the calculations showed a good qualitative agreement. The heat transfer and friction were compared to correlations for a similar configuration found in the literature. The comparison showed that the RSM results were more consistent with the experimental results than the k–ϵ results with and without wall functions © 1999 Elsevier Science Inc. All rights reserved.

Notation

A_μ	turbulence model constant
C_μ	turbulence model constant
D	height and width of passage legs, $D = 100$ mm
D_h	hydraulic diameter, $D_h = D$
f	friction factor
h	rib height
k	turbulent kinetic energy
l_μ	turbulence model constant
Re	Reynolds number
Re_y	wall-distance based Reynolds number
Nu	Nusselt number
$u'v'$	Cartesian component of turbulent shear stress
$u'w'$	Cartesian component of turbulent shear stress
u'	fluctuating velocity component in axial direction
U	mean velocity component in x direction
U_b	bulk mean-velocity
v'	fluctuating velocity component in vertical direction
V	mean velocity component in y direction
w'	fluctuating velocity component in spanwise direction
W	mean velocity component in spanwise (z-axis) direction
x	Cartesian coordinate in axial duct direction

y	Cartesian coordinate in vertical duct direction
z	Cartesian coordinate in spanwise duct direction
μ	dynamic viscosity of the fluid
μ_t	turbulent dynamic viscosity
μ_{eff}	effective dynamic viscosity
ρ	density
ϵ	dissipation rate

1. Introduction

Advanced gas turbines are designed to operate with high efficiency to decrease fuel consumption as well as the pollution of the environment. The theoretical efficiency of the gas turbine cycle rises with higher turbine pressure ratios and more importantly with higher turbine inlet temperatures. The maximum turbine inlet temperature is limited by the availability of blade material that can withstand such high temperatures and stresses. During the last 50 yr a considerable increase of the turbine inlet temperature has been achieved, e.g. Lakshminarayana (1996). Modern materials can withstand temperatures of 1100–1300 K. Present gas turbines operate at turbine inlet temperatures of approximately 1500–2000 K or more. Effective cooling is applied to the turbine components that are exposed to the hot stream. For this, a combination of internal and external cooling methods is typically employed to lower the mean blade temperature to allowable values.

For the internal cooling of the blades, the coolant is passed through a multi-pass circuit from hub to tip and ejected at the

trailing edge or the blade tip. The straight sections of these coolant passages are connected by 180° bends. To enhance heat transfer, the walls are roughened by ribs or pin fins that lead to complicated flow patterns in the passage. Numerical heat transfer predictions are not yet sufficiently accurate for design purposes that are dominated by complex turbulent transport processes. This is especially true for the complicated heat transfer patterns in the turning region of stationary or rotating coolant passages with rib roughened walls. To improve the performance of the CFD codes that will be used to evaluate a cooling configuration, a validation of the predictions is necessary and detailed measurements of the flow structure in the passages are required for comparison. The studies described in this paper support one gas turbine developers effort to understand and model the internal cooling with the expectation that better mathematical modeling will decrease airfoil design time and produce an airfoil that uses an optimally small amount of coolant flow.

1.1. Background information for numerical heat transfer and modeling of internal coolant passages

Thus, far most of the published numerical effort has been directed toward obtaining heat transfer predictions in smooth stationary and rotating coolant channels. Reviews of the efforts to predict heat transfer in these channels were presented by Iacovides and Launder (1995) and Prakash and Zerkle (1992). The reader is referred to their reviews for details of previous work and to Bo et al. (1995) for a general discussion of the code algorithms and turbulence models.Less data has been available for the comparison of the velocity and turbulent transport characteristics for flow in coolant channels with ribs. The data available was generally obtained with LDV or hot wires and was limited to traverse locations along the centerline of the passage and a limited number of other locations. Previous experiments to define the flow characteristics and to provide data for CFD evaluation have included LDV measurements in rotating and stationary two-pass passages by Cheah et al. (1994) and Iacovides et al. (1996). Liou and Chen (1997) recently performed LDV measurements of the developing flow through a smooth duct with a 180° straight-corner turn. Tse and Steuber, 1997 reported 3D LDV measurements in rotating square serpentine coolant passage with skewed ribs.

Bonhoff et al. (1996, 1997) presented a numerical/experimental comparison of the heat transfer in a two pass serpentine. These investigations included flow and heat transfer in the straight sections and the bend regions of cooling channels with smooth walls and walls with rounded ribs at an angle 45-degree to the flow direction. The results for the stationary and rotating modes were compared to experiments presented by Wagner et al. (1991) and Johnson et al. (1994). For the calculations, the FLUENT code was used with the k–ϵ model, the RNG variation of the k–ϵ model and the differential Reynolds stress model. One important conclusion from these papers was that results using the differential Reynolds stress model were consistently closer to the experimental data than those obtained using the standard or the RNG k–ϵ models. This was especially true for the turn region where the flow separates.

The velocity and turbulent transport characteristics, and therefore the heat transfer characteristics, in coolant passages with ribs are also believed to be influenced by the shape of the ribs, especially the curvature at the root and crown of the rib and the angle of the rib to the mean flow direction. The present investigation is limited to ribs with sharp corners that are typical of those in large electrical producing gas turbines.

1.2. Background information on the PIV measurement technique

In the present study, the particle-image-velocimetry (PIV) method was employed for the investigation of the flow in a model of a stationary coolant passage. PIV was chosen because of the high data acquisition rate and the good spatial resolution of the measured flow fields. These advantages, compared to LDV, are obtained because the PIV measurement obtains data from a plane in the flowfield rather than a point. The reader is referred to Grant (1994) for more references on the PIV measurement technology and a detailed discussion of the requirements for the setup of PIV experiments.

The PIV measurement technology has limitations and operational difficulties. The measurements of highly three-dimensional flow with a single-camera PIV system could have substantial errors because the out-of-plane motion of a particle perpendicular to the light sheet plane produces a systematic measurement error that increases with increasing distance from the optical axis, e.g., Lourenco (1988). An error correction for the in-plane components is feasible if the out-of-plane component of the flow is known. Schabacker and Bölcs (1996) applied the correction to single-camera 3D PIV velocity measurements and showed that the effect of the out-of-plane motion can not be corrected completely, although the correction improves the measurement accuracy.

For the present investigation, therefore a stereoscopic PIV system was assembled. In stereoscopic PIV, two cameras record the flow field from two different viewing angles. The instantaneous 3D-flow field is reconstructed from the two stereoscopic images.

More information to stereoscopic PIV can be found in Prasad and Adrian (1993) who describe optical and operational arrangements. Westerweel and Nieuwstadt (1991) have reported performance tests on three-dimensional velocity measurements with a digital two-camera stereoscopic PIV system.

The stereoscopic PIV used for the present investigation employs the angular displacement method with commercially available devices; i.e. no modifications to the cameras have been made. The small amount of defocusing of the images towards the edges was found to have a minor influence and was tolerated. The system is capable of measuring simultaneously all three-velocity components. Subsequently, an ensemble average of the velocity data in identical spatial windows is calculated leading to the mean and fluctuating velocity field.

2. Description of experiment

A sketch of the test section is shown in Fig. 1. Air was chosen as the working medium because heat transfer experiments will be conducted in the same facility in the near future. A continuously running compressor supplies the air to the test rig. Upstream of the test-rig, the mass flow rate is measured by means of an orifice meter.

The air enters the settling chamber with an inner diameter of 600 mm via a 150 mm tube and a conical entrance section with an angle of 30°. The settling chamber is equipped with a combination of perforated plates, honeycombs and meshes to reduce unsteadiness and swirl in the flow. For the PIV experiments, 1–3 μm oil droplets generated by a Polytec L2F-A-1000 Aerosol Generator are injected upstream of the settling chamber to guarantee a homogeneous seeding density in the test section.

A modular concept was chosen for the test section design that allows an easy exchange of the components. The test rig was equipped with a model of a two-pass cooling passage of a
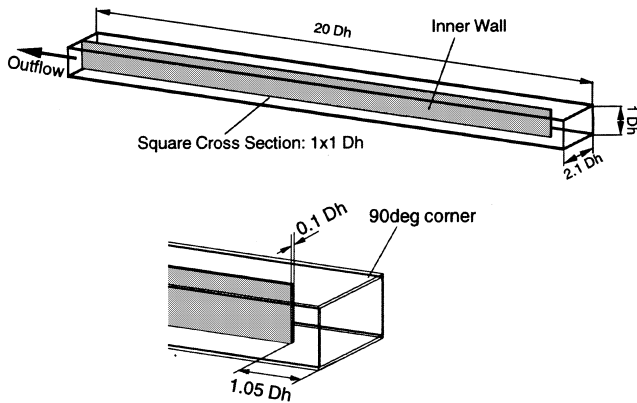
Fig. 1. The internal coolant passage test facility.

gas turbine blade. The flow path in the downstream and upstream leg had a cross-section of 100×100 mm^2 with a corresponding hydraulic diameter $D_h = 100$ mm and a length of $19 D_h$. The test section was made of 5-mm thick float glass to obtain good optical properties for the PIV experiment. The thickness of the divider plate was $0.1 D_h$. The total section including the section entrance can be turned 90° around the x-axis without changing the flow conditions in the duct. This allowed an easy optical access to the positions of interest for the PIV measurements.

A Quantel TwinsB Nd–Yag double oscillator pulsed laser provides light pulses having a maximum energy of 320 mJ at a wavelength of 532 nm. The time delay between a pair of pulses can be adjusted from 1 µs to 1 s with pulse duration of 5 ns. A plano-concave lens and two plano-cylindrical lenses, transform the beam into a thin vertical light sheet. By adjusting the distance between these lenses, the desired thickness and width of the light sheet can be obtained. The complete system including laser, light sheet optics and camera is mounted on a traversing system (Fig. 2) that allows an easy traverse to the position of interest.

A sketch of the digital PIV system is shown in Fig. 3. The system consists of two independent Kodak ES1.0 cameras each having its own PC. The ES1.0 has a CCD interline transfer sensor, which has a pixels array of 1008(H) by 1018(V) pixels. Each pixel measures nine microns square with a 60% fill factor using a micro lens. The camera outputs 8 bit digital images with 256 gray levels. The camera is used in a special double exposure frame triggering mode which allows the capture of two images separated by a delay ranging from 2 to 66 ms. For
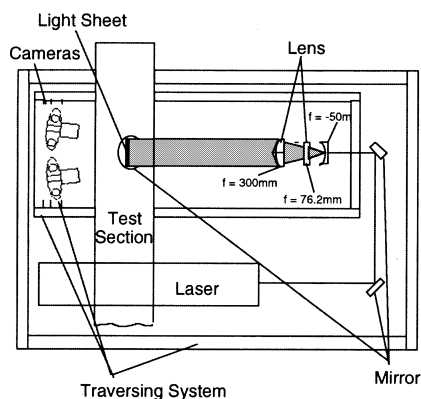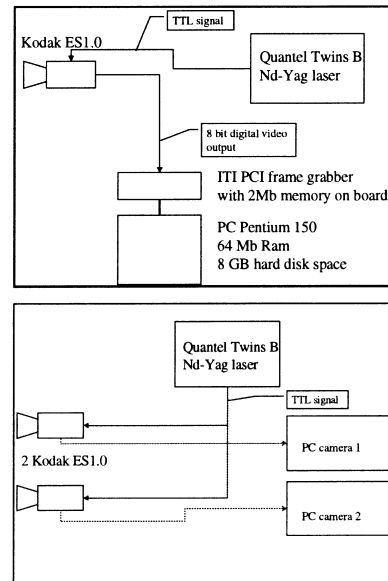

Fig. 3. Digital PIV system.

a typical recording situation, the cameras are placed with an oblique angle of 5 degree at a distance of 0.7 m from the light sheet plane.

The PIV image acquisition starts with a signal from the laser. Two images are captured in rapid succession by capturing the first image in the photo diode array, transferring this image to the CCD array and then capturing a second image in the photo diode array. The first image is transferred from the CCD to the frame grabber while the second image is being captured by the photo diode array. The second image is then transferred into the CCD array and subsequently onto the frame grabber's second image buffer. The frame grabber is an Imaging Technology PCI frame grabber with 2 MB memory onboard. The PCs are equipped with 64 MB RAM and 8 GB hard disk space. During the PIV measurement series, 50 images are written in real time into the PC's RAM memory after which the acquisition is stopped and the images are saved on the hard disk.

The PIV recordings from the right and left camera are interrogated independently with the PIV software package VISIFLOW. A cross-correlation analysis method is used with an interrogation window size of 64×64 pixels and 50% overlap between the interrogation windows. Each recording results in a 30×30 vector field of the instantaneous velocity. Usually the data contains a small number of spurious vectors (<2%). The vector field is therefore validated with predefined thresholds for the vector continuity and velocity magnitude. Vectors that do not fall within the thresholds are removed and the remaining gaps are filled by a weighted average of surrounding vectors.

From the processed vector fields, the instantaneous three-dimensional velocity field can be reconstructed. For angular PIV systems, where both cameras observe the light sheet from the same side, the corresponding interrogation positions for the two images in the plane of the light sheet do not match in general. Therefore, a calibration of the camera system is performed that also corrects for the distortion of the images in the lenses and the glass walls of the passage.

The evaluation of time-averaged turbulent transport models requires the mean-velocity field and the turbulence quantities of the flow. The statistical distribution of the velocity components is obtained from identical spatial windows

Fig. 2. PIV setup.

in a series of 200–1000 instantaneous PIV measurements. From these statistical distributions, the desired mean-velocity field and Reynolds stresses are obtained. The data requirements, uncertainty estimates and system limitations for these results are discussed further by Schabacker et al. (1998). For the present PIV measurements, the 95% confidence intervals for the mean-velocity field were determined to be between 0.025 and 0.1 U_b ($U_b = 7.65$ m/s) depending on the flow turbulence. The 95% uncertainty intervals for the fluctuating velocity components and Reynolds shear stresses were determined to be less than 0.05 U_b and 0.01 U_b^2, respectively.

3. Description of analytical model

The focus of the present analysis is on a periodic-developed flow condition, which assumes that the flow repeats itself cyclically from one rib to the next. This assumption allows the calculation domain (Fig. 4) to be limited to the region between two adjacent ribs and the computational grid contains a reasonable number of nodes.

3.1. Mathematical and numerical methods

The structured FLUENT code V 4.4.7 was used for all calculations. This program is a finite volume code using a cell centered, nonstaggered grid. The Reynolds-averaged Navier–Stokes equations and the transport equations of the turbulent quantities are solved by the pressure correction algorithm SIMPLE.

The convective scheme is upwind of second order for all equations and is used in conjunction with a limiter. Note, that the first order upwind scheme did not lead to significant differences in the results, which gives further confidence in the grid used.

During the iteration process, the sparse large linear systems of equations were solved by an iterative Line-Gauss-Seidel algorithm (LGS). When solving the pressure correction equation, a multigrid technique in combination with a one-dimensional block correction was used in order to increase the rate of convergence of the LGS algorithm.

The fluid is considered as incompressible. The fluid properties are assumed as constant. To account for turbulent effects, the Reynolds-averaged Navier–Stokes equations are considered the governing equations of the flow field.

3.2. Turbulence modeling

The main characteristics of the three semi-empirical turbulence models, used for the flow predictions, are outlined below.

The standard k–ϵ model: In this model two entities that are used for describing turbulence are introduced: the specific kinetic turbulent energy k and its dissipation ϵ. For both entities, differential transport equations are introduced which are

solved in addition to the other equations. The Reynolds-stress tensor is calculated according to the Boussinesq hypothesis and the dynamic viscosity is replaced by an effective viscosity $\mu_{\text{eff}} = \mu + \mu_t$ with $\mu_t = \rho C_\mu k^2 / \varepsilon$. C_μ is a modeling constant. A detailed description of this model can be found in Launder and Spalding (1974).

The differential Reynolds stress model (RSM): Differential transport equations are introduced for the auto- and cross-correlations of the turbulent velocities as well as for the dissipation rate ϵ. More details can be found in Launder et al. (1975).

Both the k–ϵ and the RSM turbulence models are used in combination with the logarithmic wall function to treat the wall boundary layer. The theory of turbulence modeling and a detailed description of the implementation can be found in the FLUENT manual (1995).

Two layer k–ϵ model: In the two-layer model, the whole domain is subdivided into a viscosity-affected region and a fully-turbulent region. The demarcation of the two regions is based on a wall-distance-based Reynolds number.

$$\text{Re}_y \equiv \frac{\rho \cdot y}{\mu} \sqrt{k}. \tag{1}$$

In the fully turbulent region ($\text{Re}_y > 200$), the standard k–ϵ model is employed. In the viscosity-affected near-wall region, the one equation model of Wolfstein (1969) is employed. In this model, the k equation is solved as in the standard k–ϵ model and the turbulent viscosity is computed from $\mu_t = \rho C_\mu k^{1/2} l_\mu$. The length scale l_μ is computed from

$$l_\mu = c_l y \left[1 - \exp\left(-\frac{\text{Re}_y}{A_\mu} \right) \right] \tag{2}$$

In this equation c_l and A_μ are model constants

$$c_l = \kappa \cdot c_\mu^{-3/4}$$

with $c_\mu = 0.09$ and $A_\mu = 70$, Chen and Patel (1988).

3.3. Configuration

The integration domain is shown in Fig. 4. The grid consists of about 56 000 ($45 \times 40 \times 31$) computational cells for the calculations with wall functions and of about 215 000 ($80 \times 64 \times 42$) cells for the two-layer approach. For the present calculations with cyclic boundary conditions, the only boundary conditions that are needed are the mass flow through the channel and the wall temperatures. With the constant density and viscosity, the mass flow was calculated by adjusting the Reynolds number. The wall temperature was set to a constant value of 100 K above the bulk inlet temperature.

4. Comparison of results

The computational results of the flow field are compared to the experimental data of the PIV measurements. Reference locations for the rib modules are $x = 0$ at the downstream corner of the bottom rib and $y = 0$ is located at the bottom of the channel (Fig. 5). Reference locations for PIV measurement planes perpendicular to the mean flow direction and perpendicular to the ribs are shown in Fig. 6.

4.1. Flow field in the channel

The flow between the ribs for a coolant channel with staggered ribs at 45 degrees to the mean flow direction is complex. The inclination of the ribs causes a complex 3D-vortex where the fluid is driven towards one side (called "trailing") wall by the ribs, and returns towards the opposite
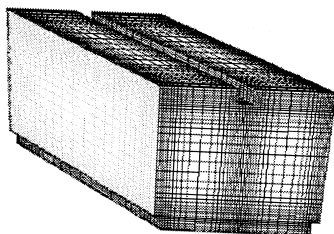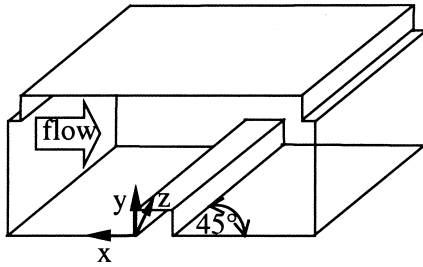

Fig. 4. Computational domain.
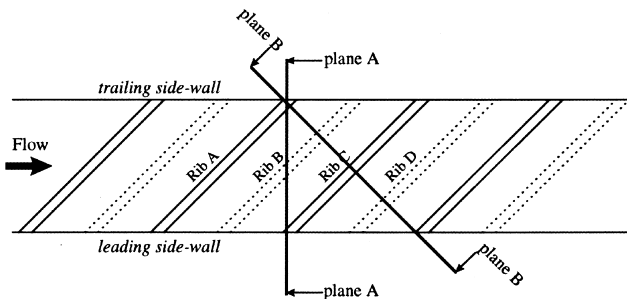
Fig. 5. Definition of coordinate system.

Fig. 6. Rib arrangement and location of slices for PIV measurements.
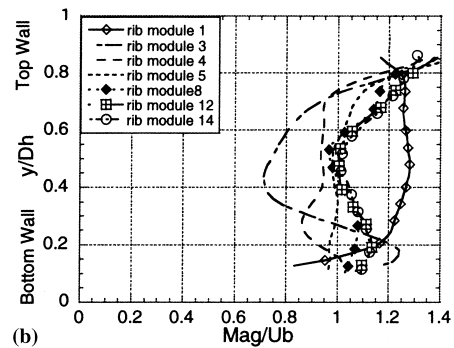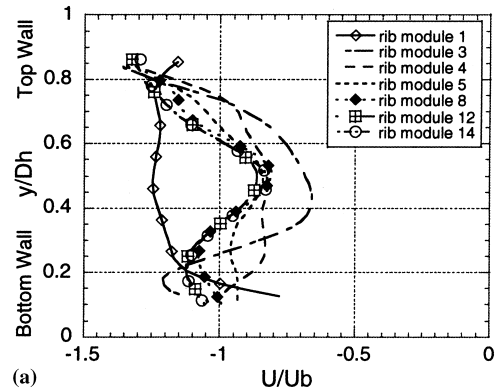

Fig. 7. Velocity profiles in the channel mid-plane at selected locations in the coolant passage. (The profiles were extracted at the mid-position of the rib on the top wall.) (a) Streamwise velocity profiles. (b) Velocity magnitude profiles.

side wall (called "leading") in the center of the channel. This secondary motion is expected to enhance the heat transfer performance and therefore, an accurate computation of the vortex structure is important.

Mean measured velocity profiles at selected distances from the inlet along the mid-plane of the channel at selected locations in the channel are presented in Fig. 7. The profiles have been plotted at streamwise locations corresponding to the center of the rib on the top wall. Detailed experimental data were only obtained between the 8th and 9th rib of the apparatus. These data were used for comparison with the numerical predicted results. From Fig. 7, it can be seen that for obtaining a near periodic flow a longer channel length is required than was necessary for tests with a 90-degree rib configuration (Schabacker et al., 1999). Because the experiment consisted of measurements in the first leg of a U-duct, the measurements from the last ribs of this leg were too close to the U-turn to be considered for our comparison purposes.

The development of the secondary motion with the 45 degree ribs produces complex velocity profiles. The streamwise velocity profiles have two maxima and one minimum at the center of the duct. The profile is different than that measured from smooth wall (Schabacker et al., 1998) or from 90-degree rib (Schabacker et al., 1999) configurations where the maximum velocity occurred in the center of the channel. This can be explained by the presence of two secondary vortices, shown later in Fig. 9, with maximal streamwise velocities in their center.

The calculations reproduce the complex flow characteristics as shown by the velocity profiles in Fig. 8. Note that the maximal streamwise velocities are over-predicted (Fig. 8(a)). However, the flow in the experiments may not be fully-developed at these locations (see Fig. 7(b)).

The spanwise velocity profiles (Fig. 8(b)) indicate the strong three-dimensionality of this flow. The flow is driven along the bottom and top wall along the ribs with a positive spanwise velocity and then returns towards the opposite side wall in the core of the channel with a negative spanwise velocity. The

intensity of this movement is reproduced by all turbulence and wall models.

The qualitative behavior of the vertical velocities (Fig. 8(c)) is reproduced by the calculations with negative velocities close to the bottom wall and the top rib. In the core of the channel, there is an upward flow. Although the three models capture this feature, they under-predict the magnitude in the center section. Note that calculations with either the RSM with wall-functions or the k–ϵ model with a two-layer approach produce the experimentally measured levels of downwards velocity. The velocity magnitude profiles in Fig. 8(d) show one effect of the ribs inclination, namely that there is a low velocity defect along the walls which is good for mixing and heat transfer performances. In addition, the maximal velocity magnitudes are located close to the ribbed walls instead of being in the core of the channel.

The enhancement of heat transfer performances with a 45-degrees inclined ribs configuration is due to the creation of large secondary vortex structures in the channel. The 2D-contours of the spanwise velocity in plane A is shown in Fig. 9. The RSM predictions are able to reproduce the secondary flow motion, both quantitatively and qualitatively (cf. Fig. 9(b)). The shapes and locations of the secondary vortices are well predicted.

A comparison between the measured and predicted secondary flow vectors (different scale) in plane A are shown in Fig. 10. The fluid is driven along the ribs close to the bottom and top walls, and in the opposite direction in the center of the channel. Coolant is convected towards the roughened walls along the leading wall, thereby enhancing the mixing process and the heat transfer performances. The predictions with the RSM model reproduce this motion both quantitatively and
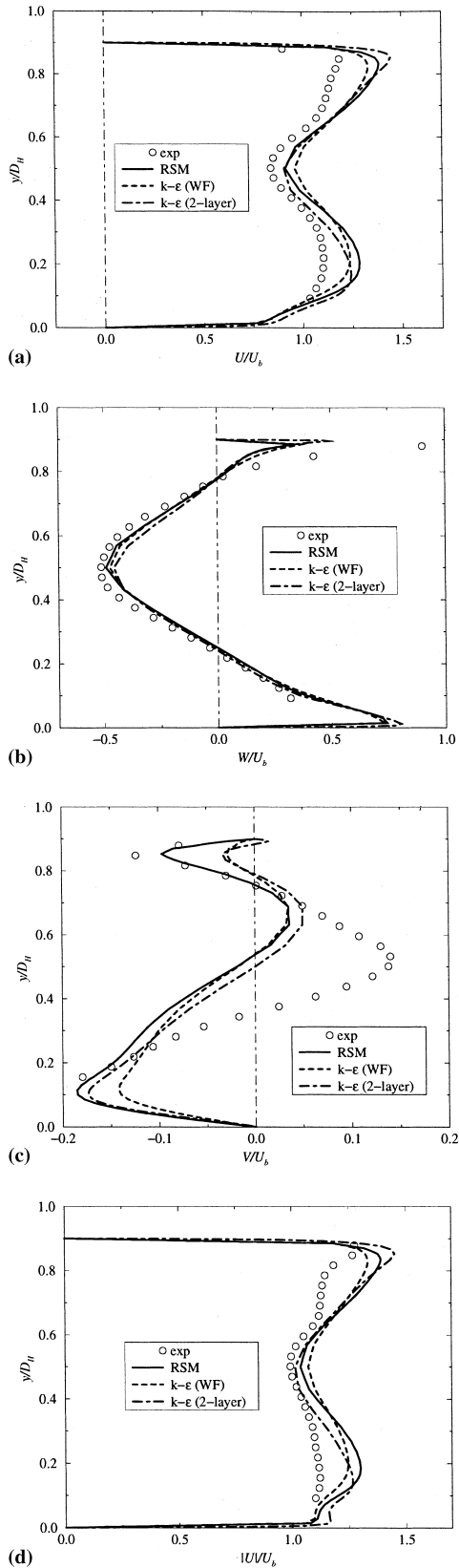
(a)

(b)

(c)

(d)

Fig. 8. Velocity profiles at $z/D = 0.5$ and a streamwise location corresponding to the middle of the top rib, Plane A, Rib B. (a) Streamwise velocity profiles. (b) Spanwise velocity profiles. (c) Vertical velocity profiles. (d) Velocity magnitude profiles.

qualitatively. Note that both the shapes and locations of the secondary vortices are well predicted. The qualitative agreement is similar to that seen in Fig. 8(a), (b), (c).

The development of the flow in plane B (Fig. 6) is shown in Fig. 11(a) and (b). The CFD simulations (Fig. 11(a)) reveal the decrease of the size of the recirculation zone or vortex behind the leading rib as the distance from the side walls increases. In particular, a rather large recirculation zone occurs downstream of Rib A close to the sidewall, whereas behind Ribs B, C, D significant smaller vortices occur. The PIV measurements (Fig. 11(b)) verify this effect. A good overall agreement between measurements and CFD simulation can be observed.

The flow reattaches at approximately two rib heights behind the Rib 9 and at approximately 3.5 rib heights behind Rib 8. The relatively small reattachment length behind Rib 9 is attributed to the secondary flows in the channel that drive fluid along the leading wall towards the inter-rib cavities.

The contour maps of the vertical velocity component (y-axis component, i.e. perpendicular to ribbed wall) are shown in Fig. 12. The velocity data was extracted in a plane at 50% rib. The downward velocity has the greatest magnitude behind rib A near the leading sidewall. These qualitative features of the flow in this local region are well reproduced by the numerical simulations (Fig. 12(a)). Nevertheless, the contours of the downwards velocity in this plane are well predicted with vertical velocities as much as 40% of the bulk velocity behind the ribs on the leading side-wall.

The average flow, especially the secondary motion is also well predicted by calculations with the k–ϵ model, with either wall functions or the two-layer approach (not shown here). The presence of the repeated ribs continuously feeds the secondary vortices. Under these conditions, the prediction of their strength depends only weakly on the turbulence model. The
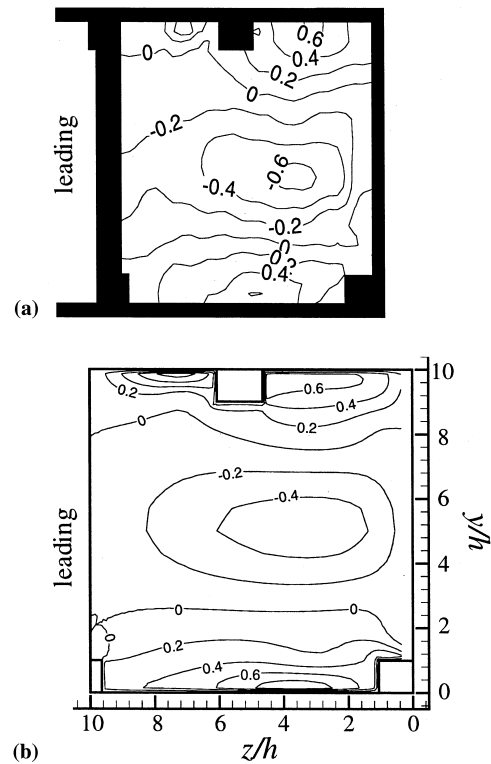

(a)

(b)

Fig. 9. Spanwise (z-axis) velocity distribution in plane A; the flow is coming out of the plane. (a) Experimentally measured. (b) Predicted with RSM model.
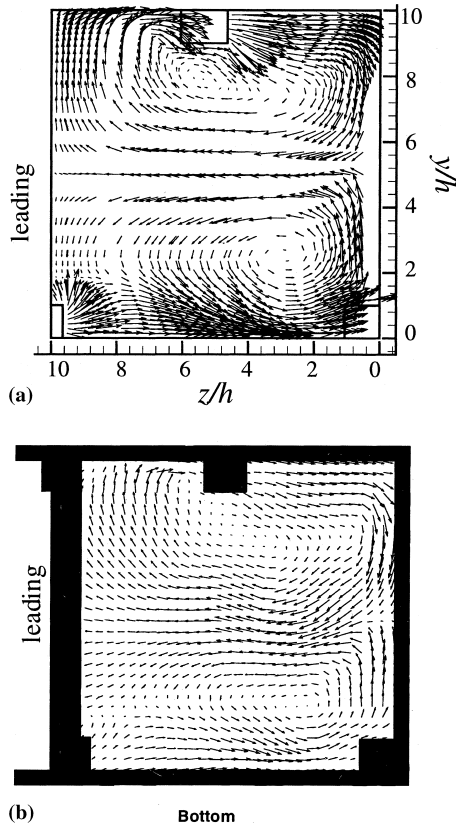
Fig. 10. Comparison of predicted and measured secondary motions in plane A (the flow is coming out of the plane). (a) Predicted with RSM model. (b) Experimentally measured.
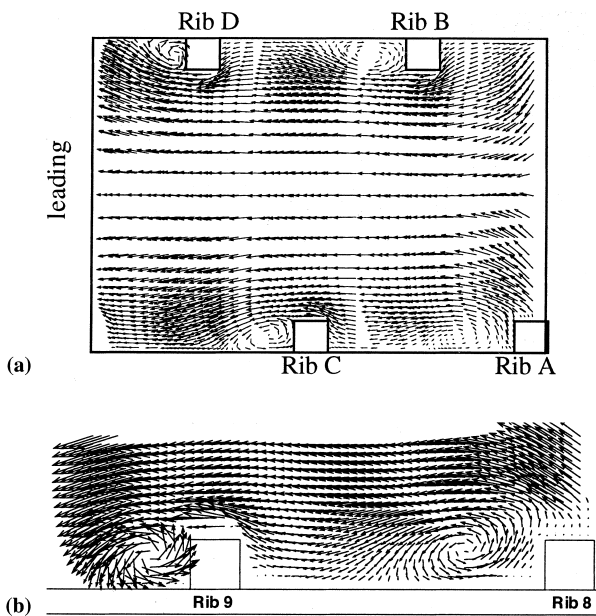

Fig. 11. Comparison of the projected flow in plane B. (a) Predicted with RSM model. (b) Experimentally measured.

misbehavior of the k–ϵ type models for predicting the evolution of secondary motions (they tend to a too rapid diffusion of these vortices) is of minor importance for this type of configuration.

4.2. Heat transfer and pressure losses

Important information for the design of a cooling system are the average heat transfer coefficients (characterized by the non-dimensional Nusselt number) and the average pressure losses (characterized by the non-dimensional friction factor) of a cooling channel. The Nusselt number has been evaluated with the volume averaged temperature as a reference temperature. The cooling efficiency is a third important parameter for cooling designs with a low-pressure loss constraint. Following previous experimental studies, Gee and Webb (1980), Han et al. (1985), one way of evaluating the performance or efficiency of a cooling system is to evaluate the ratio $(\mathrm{Nu}/\mathrm{Nu}_S)/(f/f_S)^{1/3}$, "$s$" indicating the values obtained for a smooth channel. Standard correlations are usually chosen for the smooth wall correlation, e.g., Han et al. (1985).

For comparison of the predicted heat transfer results, the Han et al. (1985) correlation for similar configurations but with non-staggered ribs (inclination angles between 30 and 90 degrees) has been chosen. Staggering the ribs is expected to show similar friction and heat transfer behavior. However, no definitive quantitative conclusion can be drawn due to these differences. The Han et al. correlation was established with a confidence of 5% for the friction factor and 10% for the Nusselt number. The predicted results for pressure drop, heat transfer coefficient and cooling efficiency obtained by the three turbulence models are tabulated in Table 1.

The predicted heat transfer and pressure drop are greater than the values from the correlation for all turbulence models. The variation between the models is also very large with the RSM results consistently closer to the correlated values. Note that the y^+ requirements were respected for both near wall approaches (except some unavoidable local too small values of
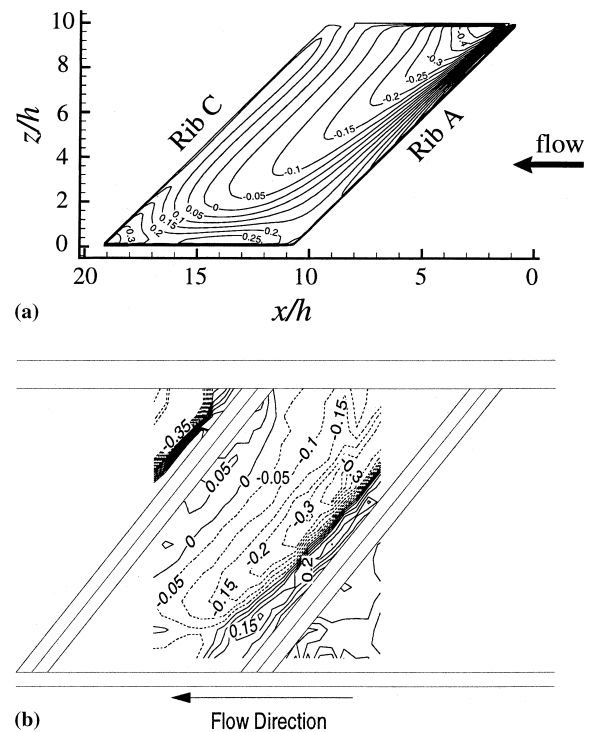

Fig. 12. Comparison of Experimental and predicted Iso-contours of the vertical velocity (y-axis) in an horizontal plane located at 50% rib height from the roughened wall. (a) Predicted with RSM model. (b) Experimentally measured.

y^+ for the wall function cases). Re_y at the first near wall grid point was less then three.

Fig. 13 shows the distribution of local Nusselt number isolines on the roughened wall with both RSM and k–ϵ models, both with the wall function approach. A more even distribution occurred for the RSM-simulation. For the k–ϵ results, there is an area of high heat transfer immediately downstream of the rib, along the "leading" sidewall. This area is located in the reattachment region, described previously. Here the flow toward the wall is high (40% of the bulk velocity), the bubble is small and its intensity is enhanced by the presence of the secondary motion in the channel. Thus, the impingement of the flow on the wall is stronger than predicted on the other side of the channel.

Fig. 14 shows a comparison of the dimensionless turbulent kinetic energy close to the wall (15% of rib height away from the wall). One can observe the similar phenomena for the two models; the k–ϵ model produces a local high turbulence spot in the same region. The same observation can be made with the two-layer approach for the k–ϵ model. Previously, k–ϵ models have predicted higher than measured levels of turbulence in impingement regions, e.g., Craft et al. (1993) and Behnia et al. (1998). This characteristic of the model may explain the difference in heat transfer even if the mean average flow is quite well reproduced by all the models. Note also that the anisotropy of near-wall turbulence increases in the inclined rib configuration, which weakens the assumed isotropic k–ϵ condition. Local heat transfer experiments will be necessary for a better assessment and more definitive conclusions regarding this coolant passage.

5. Concluding remarks

In the present paper, a stereoscopic PIV system has been employed for the measurement of the turbulent flow characteristics in a model of a gas turbine coolant passage. The PIV technique was shown capable of obtaining velocity measurements with a high spatial resolution and a reasonably small uncertainty of the results. The data acquisition rate was high and thus allowed for a fuller investigation of the flow in a complex geometry where many measurement planes are required to obtain a comprehensive understanding of the flow phenomena and a large database for the evaluation of turbulence models for CFD codes. From the statistical distribution of the velocity components, the mean-velocity field and turbulent transport of the flow were calculated. The velocity fields were arranged on a regular grid and can therefore ideally be used to evaluate CFD simulations.

Numerical simulations have been performed for the experimental flow and geometric conditions with three different turbulence models: (i) the k–ϵ model with both wall functions and (ii) a two-layer approach, and (iii) the RSM model with wall functions. Comparison of the predicted flows with measurements showed a generally good agreement. The complex flow features, namely the recirculation zones and vortices behind the ribs and the secondary motion through the channel
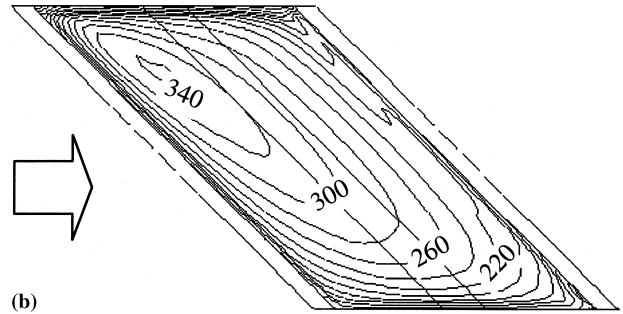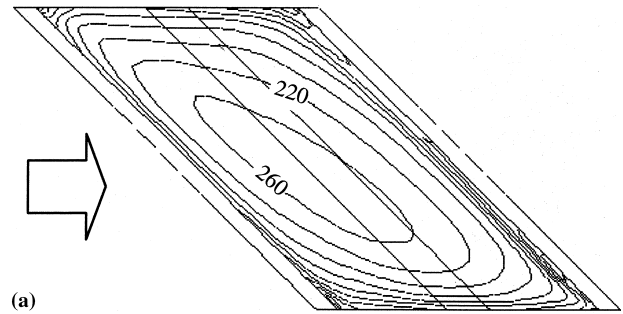

Fig. 13. Nusselt numbers on wall. (a) RSM turbulence model. (b) k–ϵ turbulence model.
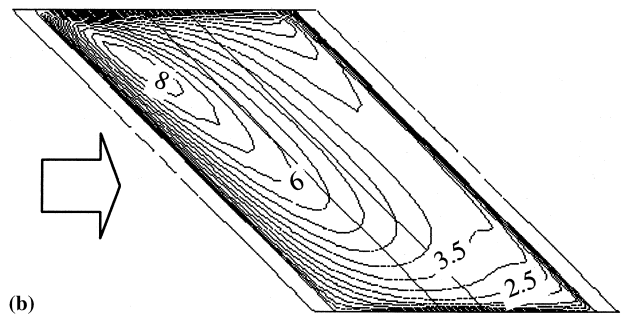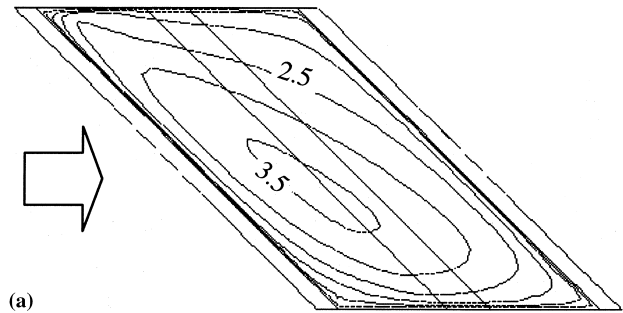

Fig. 14. Iso contours of k/U_b^2 ($\times 10^{-2}$) distribution at distance equal 15% rib height from the wall. (a) RSM turbulence model. (b) k–ϵ turbulence model.

were predicted. A global analysis of the results showed a slight preference for the RSM model, although the differences are not as high as expected. The grid used for the calculations represented the limit of the applicability range of the wall function with regard to resolving the near wall flow. A smaller Reynolds number or smaller rib heights would lead to too small y^+ – values near the wall. Some larger differences in the predicted results between the models were found close to the solid

Table 1
Friction factor, Nusselt number and efficiency for one roughened-channel period

	Han et al. correlation	RSM WF	k–ϵ WF	k–ϵ 2 layer
f	4.6×10^{-2}	6.0×10^{-2}	6.5×10^{-2}	6.4×10^{-2}
Nu	256.2	290	350.5	377.5
η	1.23	1.27	1.50	1.62

boundaries, especially in predicted turbulence levels. These differences lead to different wall heat transfer distributions and pressure losses. The RSM velocity distributions predictions were consistent with the experimental data and returned reasonable ratios of heat transfer efficiency. The k–ϵ model, with both wall functions and a two-layer model, predicted greater heat transfer and pressure losses than the RSM. The near-wall anisotropy of turbulence and impingement zones are expected to be important and may explain the k–ϵ model results.

A combined two layer wall model and a Reynolds stress model or a three equation turbulence model (Behnia et al., 1998) could provide the physical modeling required to reproduce the qualitative accuracy desired for the design and evaluation of complex coolant passages. For further investigations, near-wall turbulence and heat transfer data from the same test section are needed to make a better assessment of numerical heat transfer prediction methods for complex coolant channels.

Acknowledgements

References

Behnia, M., Parneix, S., Durbin, P., 1998. Prediction of heat transfer in an axisymmetric turbulent jet impinging on a flat plate. Int. J. Heat and Mass Transfer 41 (10), 1845–1855.

Bo, T., Iacovides, H., Launder, B.E., 1995. Convective discretisation schemes for the turbulence transport equations in flow predictions through sharp U-bends. Int. J. Num. Methods for Heat and Fluid Flow 5, 33–48.

Bonhoff, B., Tomm, U., Johnson, B.V., 1996. Heat transfer predictions for U-shaped coolant channels with skewed ribs and with smooth walls, ASME 96-TA-007, ASME Turbo Asia, Jakarta, Indonesia.

Bonhoff, B., Tomm, U., Johnson, B. V., Jennions I., 1997. Heat transfer predictions for rotating U-shaped coolant channels with skewed ribs and with smooth walls, ASME paper 97-GT-162.

Cheah, S.C., Iacovides, H., Jackson, D.C., Li, H., Launder, B.E., 1994. LDA investigation of the flow development through rotating U-ducts, ASME paper 94-GT-226.

Chen, H.C., Patel, V.C., 1988. Near-wall turbulence models for complex flows including separation. AIAA J. 26, 641–648.

Craft, T., Graham, L., Launder, B., 1993. Impinging jet studies for turbulence model assessment-II An examination of the performance of four turbulence models. Int. J. Heat and Mass Transfer 36 (10), 2685–2697.

FLUENT User's Guide, 1995, version 4.3, vol. I–IV, Fluent Deutschland GmbH.

Gee, D.L., Webb, R.L., 1980. Forced convection heat transfer in helically rib-roughened tubes. Int. J. Heat and Mass Transfer 23, 1127–1136.

Ian Grant (Ed.) 1994. Selected Papers on Particle Image Velocimetry, Spie Milestone Series, MS 99.

Han, J.C., Park, J.S., Lei, C.K., 1985. Heat transfer enhancement in channels with turbulence promoters. Journal for Engineering for gas turbines and power, 107, 628–635.

Iacovides, H., Launder, B.E., 1995. Computational fluid dynamics applied to internal gas-turbine cooling: a review. Int. J. Heat Fluid Flow 16, 454–470.

Iacovides, H., Jackson, D.C., Li, H., Kelemenis, G., Launder, B.E., Nikas, K., 1996. LDA study of the flow development through an orthogonally rotating U-bend of strong curvature and rib roughened walls, ASME paper 96-GT-476.

Johnson, B.V., Wagner, J.H., Steuber, G.D., Yeh, F.C., 1994. Heat transfer in rotating serpentine passages with trips skewed to the flow. ASME J. Turbomachinery 116, 113–123.

Lakshminarayana, B., 1996. Fluid Dynamics and Heat Transfer of Turbomachinery, Wiley, NY.

Launder, B.E., Spalding, D.R., 1974. The numerical computation of turbulent flows. Comput. Methods Appl. Mech. Engrg. 3, 269–289.

Launder, B.E., Reece, G.J., Rodi, W., 1975. Progress in the development of a Reynolds stress turbulence closure. J. Fluid Mech. 68 (3), 537–566.

Liou, T., Chen, C., 1997. LDV study of developing flows through a smooth duct with a 180° straight-corner turn, ASME paper 97-GT-283.

Lourenco, L.M., 1988. Some comments on particle image displacement velocimetry, Von Karman Institute for Fluid Dynamics, Lecture Series 1988-06.

Prakash, C., Zerkle, R., 1992. Prediction of turbulent flow and heat transfer in a radial rotating square duct. ASME J. Turbomachinery 114, 835–846.

Prasad, A.K., Adrian, R.J., 1993. Stereoscopic particle image velocimetry applied to liquid flows. Experiments in Fluids 15, 49–60.

Schabacker, J., Bölcs, A., 1996. Investigation of turbulent flow by means of the PIV method, paper presented at the 13th Symposium on Measuring Techniques for Transonic and Supersonic Flows in Cascades and Turbomachines, Zurich, Switzerland, 5–6 September.

Schabacker, J., Bölcs, A., Johnson, B.V., 1998. PIV investigation of the flow characteristics in an internal coolant passage with two ducts connected by a sharp 180° bend, ASME Preprint 98-GT-544, Stockholm, Sweden, June 1998.

Schabacker, J., Bölcs, A., Johnson, B.V. PIV investigation of the flow characteristics in an internal coolant passage with 90° rib-arrangement, Paper to be presented at Third European Conference on Turbomachinery Fluid Dynamics and Thermodynamics 2–5 March 1999, London, UK.

Tse, D.G.N., Steuber, G.D., 1997. Flow in a rotating square serpentine coolant passage with skewed trips, ASME paper 97-GT-529.

Wagner, J.H., Johnson, B.V., Kopper, F.C., 1991. Heat transfer in rotating serpentine passages with smooth walls. ASME J. Turbomachinery 113, 321–330.

Westerweel, J., Nieuwstadt, F.T., 1991. Performance tests on 3-dimensional velocity measurements with a two-camera digital particle-image-velocimeter. Laser Anemometry 1, 349–355.

Wolfstein, M., 1969. The velocity and temperature distribution of one-dimensional flow with turbulence augmentation and pressure gradient. Int. J. Heat Mass Transfer 12, 301–318.